



Full length article

A method to manipulate non-steady-state columnar-to-equiaxed transition in powder bed fusion additive manufacturing using an electron beam

Yuchao Lei^{a,b}, Kenta Aoyagi^{b,*}, Akihiko Chiba^b^a Department of Materials Processing, Graduate School of Engineering, Tohoku University, Sendai 980-8579, Japan^b Institute for Materials Research, Tohoku University, Sendai 980-8577, Japan

ARTICLE INFO

Article history:

Received 21 September 2021

Revised 27 January 2022

Accepted 2 February 2022

Available online 3 February 2022

Keywords:

Powder bed fusion additive manufacturing

Solidification

Columnar-to-equiaxed transition

Crystallographic texture

Superalloy

ABSTRACT

Site-specific control of solidification grain structure is one of the largest attractiveness of manufacturing metallic parts with powder bed fusion additive manufacturing. In this study, we manufacture non-weldable superalloy Alloy713ELC with powder bed fusion additive manufacturing using an electron beam (PBF-EB) and achieve various bulk solidification grain structures, i.e. near fully equiaxed structure, interlocked zigzag structure, and columnar structures with various grain widths, through controlling process parameters under a line order scan strategy. An analytical transient model, which is capable of simulating heat transfer in PBF-EB single-layer melting under the experimental conditions, is established and validated by compared to numerical models of computational fluid dynamics and finite element method in PBF-EB single-track melting. The evolutions of solidification grain structure are rationalized using microstructural characterization and simulations based on various models. It is found that the mechanisms of columnar grain refinement and columnar-to-equiaxed transition (CET) are related to the Walton and Chalmers selection effect, which is governed by the spatial and temporal variations of solidification direction, and to the effect of convection within mushy zone. Based on the grain structure evolution mechanisms, we propose a method to manipulate CET or to achieve a novel interlocked zigzag grain structure in PBF-EB.

© 2022 Acta Materialia Inc. Published by Elsevier Ltd. All rights reserved.

1. Introduction

Metal additive manufacturing is a rapidly emerging technology with enormous potential [1]. Among the various categories, powder bed fusion additive manufacturing (PBF-AM) has evolved to satisfy some commercial applications especially in the aerospace industry due to its advantages comparing to the conventional processes, i.e. enable manufacturing lightweight components with novel optimized geometries leading to performance benefit, and reduce cost by decreasing the buy-to-fly ratio and the cradle-to-gate environmental footprints [2].

Site-specific control of solidification grain structure satisfying the optimization of structural properties is one of the largest attractiveness of PBF-AM. This topic has been recently of great interest in powder bed fusion additive manufacturing using an electron beam (PBF-EB), which is one of the PBF-AM technologies. Because columnar grains oriented along building direction can be

easily achieved in PBF-EB due to the competitive growth, the major challenges are to produce bulk single crystal with maximized creep resistance for applications under elevated temperatures, and to produce bulk equiaxed grain structure with isotropic mechanical properties for applications under multidirectional stresses, through manipulating process parameters.

Currently, only limited kinds of approaches have been reported for site-specific control of solidification grain structure in PBF-EB. For instance, Körner et al. [3,4] and Chauvet et al. [5] have fabricated bulk single crystals of Ni-base superalloys. Fernandez-Zelaia et al. [6] later studied the process window that enables generating single crystals of Ni-base superalloys. On the other hand, to the best of our knowledge, there are presently two kinds of methods to achieve bulk equiaxed solidification grain structure in PBF-EB through controlling process parameters. Körner et al. [7,8] have obtained near equiaxed grains with relatively weak $\langle 001 \rangle$ texture aligned along building and scanning directions, through employing a cross snake scan strategy to vary solidification directions between successive layers. Dehoff et al. [9] have demonstrated the feasibility of another method to produce equiaxed grains with highly weak texture, i.e. employing point heat source

* Corresponding author.

E-mail address: kenta.aoyagi.e7@tohoku.ac.jp (K. Aoyagi).

Table 1

Process and simulation parameters of the conditions C1, C2, and E0. I, V, FO, LO, and r_b denote current, scan speed, focus offset, line offset, and nominal beam radius, respectively. NLH and TIP denote no latent heat and temperature-independent properties, respectively.

	I, mA	V, mm/s	FO, mA	LO, mm	Line order	r_b , μm	Energy absorption efficiency (η), %				
							CFD	FEM	FEM		ATM
									NLH	NLH+TIP	
C1	9.4	500	18	0.18	11	400	95	60	40	40	35
C2	2	150	3	0.23	7	260	80	50	–	–	33
E0	4	800	30	0.08	50	540	85	–	–	–	34

scan strategies. Through generating equiaxed grains that outline intricate geometries, this method has been demonstrated to be capable of achieving site specific control of solidification grain structure [10,11]. Raghavan et al. [12] have studied the bulk columnar-to-equiaxed transition (CET) induced by the point heat source scan strategy via numerical simulations. Kontis et al. [13] have demonstrated that producing bulk equiaxed grain structure also contributes to avoiding hot cracking in non-weldable Ni-base superalloy. Besides, Raghavan et al. [14] and Zhao et al. [15] have rationalized the variations in columnar grain size under various scan strategies.

In this study, we propose a method to manipulate CET in PBF-EB via a line order scan strategy. This method employs a moderately defocused electron beam and an optimized line order scan strategy with small line offset in order to make use of the spatial and temporal variations of solidification direction within each melt layer. We demonstrate that this method is capable of inducing non-steady-state CET, and as a result, creates a bulk equiaxed grain structure with a significantly weaker texture comparing to that reported by Körner et al. [7,8].

Our previous studies have focused on the high-dimensional process optimization [16] and cracking mechanisms [17] in PBF-EB built non-weldable Ni-base superalloy Alloy713ELC. In this study, the solidification grain structure evolution mechanisms are studied via an approach based on experiments and various physical models, which consider multi-physics in single-track melting or only heat transfer in single-layer melting.

2. Methodology

2.1. PBF-EB and single-track melting experiments

Pre-alloyed gas-atomized powders ($d_{50} = 90.3 \mu\text{m}$) of Alloy713ELC with chemical composition as reported in a previous study [16] were applied into an ARCAM EBM® A2X system operating at 60 kV accelerating voltage. Cuboidal samples with horizontal section dimensions $10 \times 10 \text{ mm}$ and height $35 \sim 43 \text{ mm}$ were manufactured on stainless SUS304 plates under a controlled 0.2 Pa helium atmosphere with the layer thickness and preheating temperature of $100 \mu\text{m}$ and $1000 \text{ }^\circ\text{C}$, respectively. The PBF-EB process is governed by five major process parameters, i.e. current, scan speed, focus offset, line offset, and line order. The electron beam with power proportional to the current, exhibiting approximately a surface Gaussian distribution as a function of the focus offset, is deflected to generate a melt pool with its thermal center moving at the scan speed along a linear melt track. Under the line order scan strategy, which is capable of dispersing input energy, the spacing between adjacent melt tracks and the sequence of melt tracks are determined by the line offset and the line order respectively (see Fig. A3(a) in [17] for illustration). Three sets of process parameters C1, C2, and E0 as listed in Table 1, which are optimized via a support vector machine (SVM) based high-dimensional process optimization method proposed by Aoyagi et al. [16,18], were used to fabricate PBF-EB samples with various solidification grain

structures. The process conditions C1 and C2 have been denoted as P1 and P4, respectively, in a previous study [17]. All the 3 process conditions drew on SVM optimized line order scan strategies and contours were melted before hatching. The automatic mode controlling scan speed during selective melting was turned off. The scanning directions are opposite between adjacent melting tracks in each layer and were rotated by 90° about the building direction axis between the n th and $n + 1$ th layers.

Dense plates of Alloy713ELC with fine isotropic grain structures and dimensions of approximately $15 \text{ mm } \phi \times 5 \text{ mm}$ were fabricated using spark plasma sintering (SPS) with a 5 min holding time under a uniaxial pressure of 80 MPa, a temperature of $1100 \text{ }^\circ\text{C}$, and a high-level vacuum atmosphere. The SPS process applied a DR.-SINTER Model SPS-1050 (Sumiseki Materials Co., Ltd) equipped with a graphite die, and raw powders with diameters small than $50 \mu\text{m}$ approximately, which were remained after filtering the powders used in PBF-EB. After grinding the plate surfaces on 1200-grit SiC paper and cleaning in an ultrasonic bath, single-track melting experiments were conducted on the plates under various single-track melting conditions as mentioned in Appendix A.1. The plates are carefully adjusted to keep their top surfaces at a same horizontal plane before preheating. The melting tracks on each plate were set to be sufficiently far from the adjacent ones and the plate boundaries in order to approximate melting on a half-infinite substrate, through considering thermal penetration depth. An unused filament was employed in the single-track melting experiments to exclude the effect of filament aging on actual emission current.

Specimens for microstructure characterization were sectioned along the central vertical section normal to scanning direction from the PBF-EB samples and single-track melted samples. Scanning electron microscopy photos in the backscattering electron mode (SEM-BSE; Hitachi S-3400 N) were utilized to quantify the width and depth of melt regions in the single-track melted samples. Field emission scanning electron microscopy (FE-SEM; FEI XL30S-FEG) equipped with an electron backscatter diffraction (EBSD; TexSEM Lab, TSL) detector was used to characterize solidification grain structures in PBF-EB samples. The EBSD data was analyzed with the OIM software (EDAX-TSL).

2.2. Analytical transient model

The application of analytical transient model (ATM) in PBF-AM, first reported by Plotkowski et al. [19], has been recently extensively studied in [20,21,22,23]. The basic idea of the ATM applied in this study is to integrate an analytical transient solution of a ring heat source [24]:

$$T(x, y, z) = T_0 + \frac{q}{c\rho(4\pi a)^{1.5}} \int_{\tau_i=0}^{\tau_i=t} \frac{1}{\tau^{1.5}} \exp\left(-\frac{r_0^2 + x^2 + y^2 + z^2}{4a\tau}\right) \cdot I_0\left(\frac{r_0}{2a\tau} \sqrt{x^2 + y^2}\right) d\tau_i \quad (1)$$

where T_0 is the initial temperature, q absorbed power, c specific heat, ρ density, a thermal diffusivity, τ_i integration time variable, t time of interest, and r_0 radius of ring heat source. An ATM simulation code, which had been developed to simulate heat accumulation behavior in our previous study [17], was upgraded to reveal the dependence of solidification behaviors on process parameters. Multiple concentric ring heat sources were superimposed to simulate a surface Gaussian heat source. The scan path and the nominal beam radius defined in Section 2.3 were uniformly discretized in time and distance, respectively. The integration steps of time and nominal beam radius were determined via sensitivity analysis as will be mentioned in Section 3.2.

2.3. Numerical and analytical simulations

A computational fluid dynamics (CFD) model, which was established using the Flow-3D software and Flow-3D Weld module (Flow Science, Inc) [17,25], was employed to simulate single-track melting on a half-symmetry solid plate of Alloy713ELC under the 3 process conditions C1, C2, and E0. The CFD simulation considers heat transfer, fluid flow, vaporization, radiation, latent heat, and temperature-dependence of material properties. All the simulations in this study employ a surface Gaussian heat source with the nominal beam radius defined as $r_b = \sqrt{6}\sigma$, wherein σ is the standard deviation, indicating 98.6% energy accumulates at $r < r_b$. The nominal beam radius (r_b) and energy absorption efficiency (η) for the 3 process conditions were determined to satisfy that the CFD simulated melt region dimensions fit optimally with the experimental results through trial and error.

In addition, a finite element method (FEM) model reported in our previous study [17], which considers heat transfer, fusion latent heat, temperature-dependence of material properties but ignore fluid flow, vaporization, and radiation, was also employed to simulate single-track melting under the process conditions C1, C2, and E0. Besides, the up-mentioned ATM was employed to simulate both single-track and single-layer melting under the 3 conditions.

Here we define a solidification stage of interest (SSOI) as the solidification temperature range that corresponds to solid fraction 0 ~ 66% under equilibrium solidification (equivalent to solid fraction 0 ~ 50% under Scheil solidification as calculated in [17]). The thermal gradient (G) and cooling rate (CR) within mushy zone during the SSOI were calculated using finite difference method, and solidification rate (R) was calculated as $R = CR/G$ in the 3 kinds of simulations CFD, FEM, and ATM. Only the G and R during the last solidification event were calculated in the ATM single-layer melting simulations. The calculation of cooling rate in CFD and FEM simulations applied differential time of $dt = 1 \times 10^{-4}$ s and $dt = 3 \times 10^{-4}$ s, respectively, which enables at least one time step involved during the SSOI for each mesh. The calculation of cooling rate in ATM employed the integration time steps of $dt = 3 \sim 10 \times 10^{-5}$ s as differential time. Because the small differential time in ATM and CFD enables capturing the temporal variations in G and R at each mesh, we calculate G and R with two kinds of measures, i.e. the transient measure at a specific time step and the averaged measure during the SSOI. The averaged G and R are calculated as the numerical average value of data captured at each time step during the SSOI. If G and R are not specifically noted as averaged data or as transient data at each time step during the SSOI, G and R refer to transient data when temperature first falls below equilibrium liquidus in the following article. The mesh size for the melt regions is 5~10 μm in the ATM and CFD simulations, and that in the FEM simulations applied a mesh size of 20 μm . The physical material properties applied in the simulations are written in Appendix A.2.

3. Results

3.1. Solidification grain structures

Fig. 1(a) shows the inverse pole figure (IPF) maps captured on central vertical sections at approximately 2 mm below top surfaces of the PBF-EB samples. The PBF-EB samples C1 and C2 exhibit coarse and fine columnar grain structures, respectively. The columnar grain widths of C1 and C2 are 107 and 47 μm , respectively, as reported in [17]. The PBF-EB sample E0 exhibits a near fully equiaxed grain structure. Fig. 2(a-b) show the area fraction of grains in the PBF-EB sample E0 as a function of diameter (circle equivalent diameter) and aspect ratio of grains, respectively, calculated from the EBSD scanned area in Fig. 1(a). Although 2.7% areas in the PBF-EB sample E0 exhibit grain diameters of 200 ~ 300 μm , the area fraction weighted (AFW) average grain diameter is 90 μm and the numerical average grain diameter is 48 μm , indicating E0 possesses a significantly refined solidification grain structure. The numerical average grain diameter is much smaller than that of the AFW because of the existence of a large number of fine grains. The PBF-EB sample E0 exhibits an AFW average grain aspect ratio of 0.46. The AFW average measure of the grain diameter and the aspect ratio should be able to reflect the characteristics of the bulk solidification grain structure better than the numerical average measure.

Fig. 1(b-d) show the pole figures corresponding to the building direction calculated from the EBSD scanned areas in the PBF-EB samples. The PBF-EB samples C1 and C2 exhibit strong $\langle 001 \rangle$ texture in the building direction, and their maximum values of multiple of uniform density (MUD) are 19.1 and 14.3, respectively. The PBF-EB sample C2 has a relatively stronger $\langle 001 \rangle$ texture in the scanning directions than C1. The PBF-EB sample E0 exhibits a very weak $\langle 001 \rangle$ texture in building direction with a maximum MUD of 2.87, which is close to the completely equiaxed grain structure with a MUD of near 1, indicating that the sample E0 has a near fully equiaxed grain structure.

3.2. Single-track melting

Our objective is to rationalize the variations in solidification grain structure resulted from the various process conditions. Because the effect of heat accumulation on solidification behavior is unneglectable, as will be mentioned in Section 5.1, we need to simulate the single-layer PBF-EB process under various process conditions. It is known that the CFD simulation, which calculates thermal field within melt pool by coupling the effects of multiphysics including heat transfer, fluid flow, vaporization, radiation, latent heat, and temperature-dependence of material properties, is a desired candidate for investigating the solidification grain structure evolution mechanisms. However, since the CFD simulations consume unacceptable computing costs to simulate single-layer PBF-EB process, especially in the case of the condition E0 which includes over 100 melting tracks in each layer, we consider solving this problem via ATM. In order to reveal the dependence of solidification behavior on process conditions via ATM, it is necessary to capture the electron beam characteristics under the various process conditions and to optimize the simulation parameters applied in ATM. Under these circumstances, our approach is to capture the nominal beam radius and energy absorption efficiency for the 3 process conditions by fitting the CFD simulated single-track melt region dimensions to the experimental results, as mentioned in Section 2.3.

Fig. 3(a-b) show the single-track melt regions under the conditions C1 and C2 determined via CFD simulations and experiments. The nominal beam radius and energy absorption efficiency are determined to be $r_b = 400$ μm , $\eta = 95\%$ for the condition C1 and

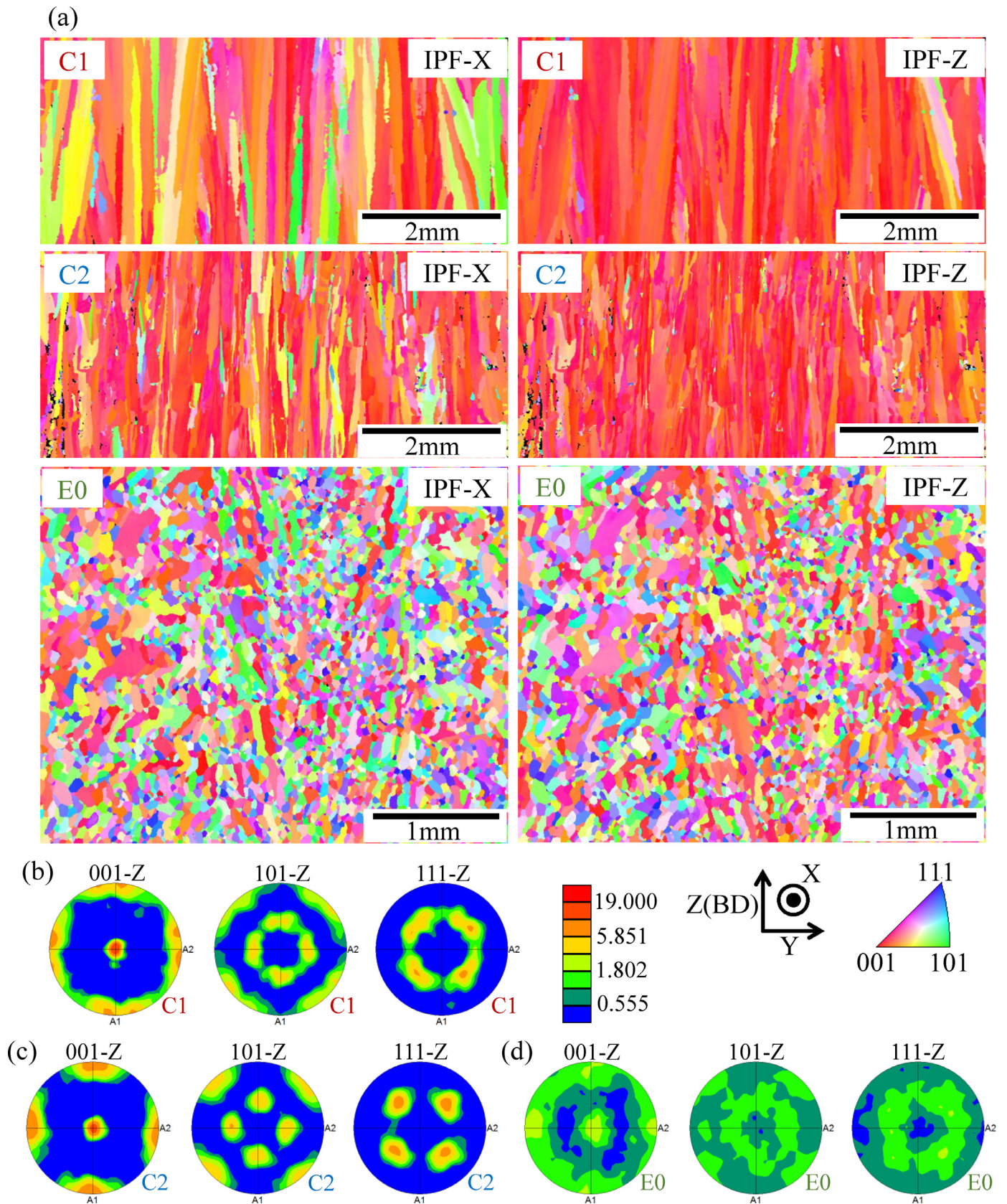


Fig. 1. (a) Inverse pole figure (IPF) maps of central vertical sections at approximately 2 mm below top surfaces of the PBF-EB samples C1, C2, and E0 with reference to scanning direction (IPF-X) and building direction (IPF-Z). Pole figures of PBF-EB samples (b) C1, (c) C2, and (d) E0 with reference to building direction. The pole figures are calculated from the IPF maps in (a). BD denotes building direction. Scanning directions are parallel with X and Y directions.

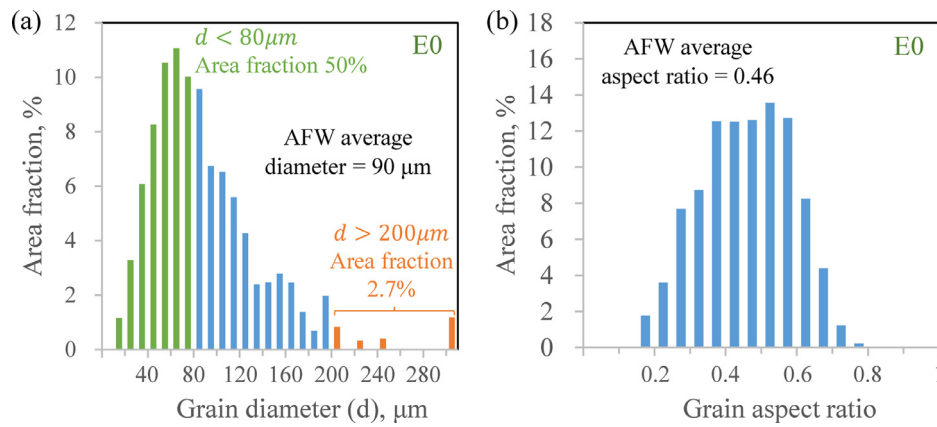


Fig. 2. Area fractions of grains as a function of (a) grain diameter (circle equivalent diameter) and (b) grain aspect ratio in the PBF-EB sample E0 with a near fully equiaxed solidification grain structure. The results are calculated from the EBSD scanned areas in Fig. 1(a). AFW denotes area fraction weighted.

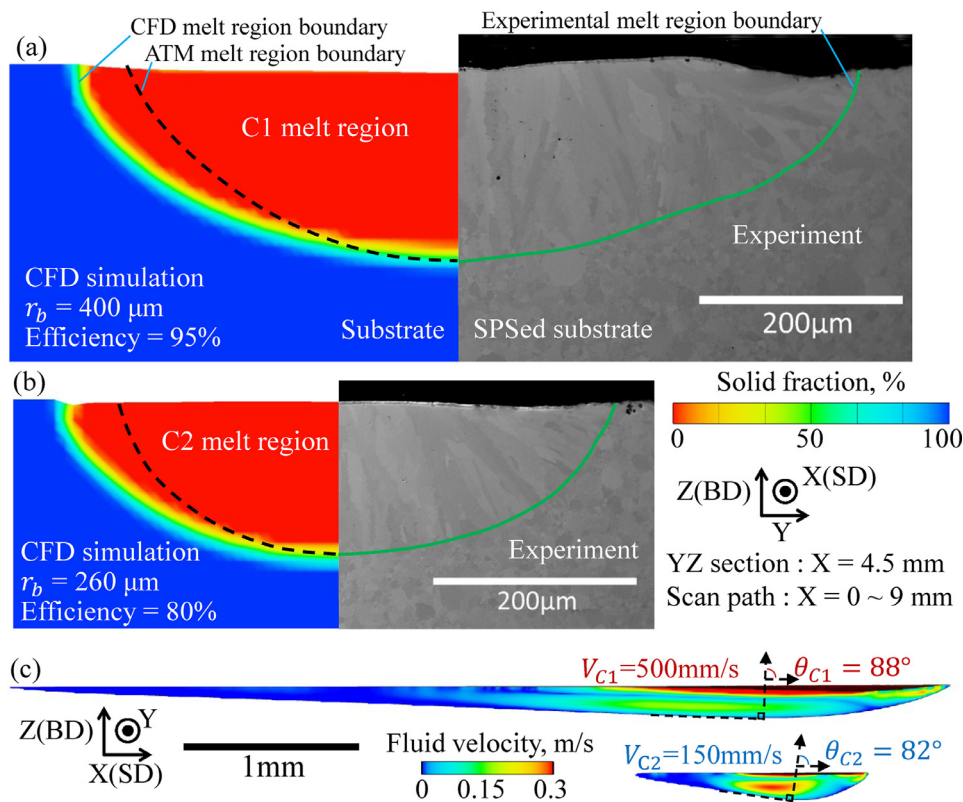


Fig. 3. Results of CFD single-track melting simulations under the conditions C1 and C2, which lead to columnar grain structures with various grain widths. (a-b) CFD simulated melt region on central sections normal to scanning direction fitted to experimental results. The black broken lines and green lines in (a-b) indicate the melt region boundaries determined via ATM and experiment respectively. (c) Transient fluid velocity magnitude mapped on central sections normal to offset direction (Y+), when the shape of both melt pools reach almost constant. BD and SD denote building and scanning directions respectively. (For interpretation of the references to color in this figure legend, the reader is referred to the web version of this article.)

$r_b = 260 \mu\text{m}$, $\eta = 80\%$ for the condition C2, as listed in Table 1, in the CFD simulations. Fig. 3(c) shows the central section of melt pool normal to offset direction (Y+) simulated with CFD under the conditions C1 and C2. The shape of both melt pools reach almost constant during single-track melting in CFD simulations. The condition C2 with smaller scan speed and power to scan speed ratio (P/V) leads to a much shorter melt pool with a steeper bottom than C1. On the other hand, the condition E0 experimentally results in an extremely shallow single-track melt region, as shown in Fig. A3(f). This leads to difficulties in determining nominal beam radius and energy absorption efficiency for the condition E0, and therefore, an extrapolated nominal beam radius $r_b = 540 \mu\text{m}$ and

an energy absorption efficiency $\eta = 85\%$ are determined for E0, as listed in Table 1. Details about determining electron beam characteristics are written in Appendix A.1.

The nominal beam radius values determined above were then applied in single-track melting simulations based on FEM and ATM in order to determine effective energy absorption efficiencies that lead to melt region depth fitting optimally with the experimental results under the 3 process conditions. The ATM and FEM simulations have multiple limitations which will be discussed in Section 4 while the CFD simulation does not have such limitations, and then, the effective energy absorption efficiencies in ATM and FEM are lower than those in CFD as shown in Table 1. The condi-

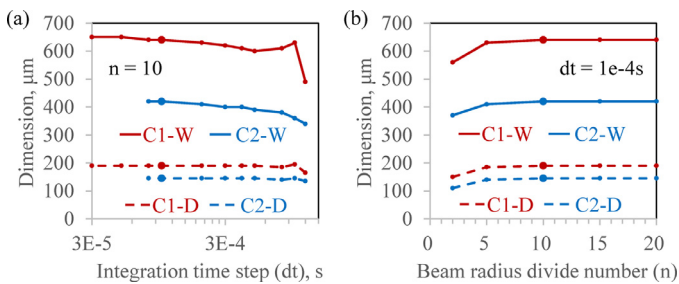


Fig. 4. Sensitivity of width (W) and depth (D) of single-track melt region to (a) integration time step dt and (b) beam radius divide number $n = r_b / dr$ in ATM single-track melting simulations under the conditions C1 and C2.

tions with larger current exhibit larger energy absorption efficiencies in the 3 different simulations, indicating that energy absorption efficiency in PBF-EB is actually as a function of beam current.

In addition, because the accuracy of ATM simulation is also dependent on the integration parameters [19], we investigated the sensitivity of single-track melt region dimensions to integration time step dt and beam radius divide number $n = r_b / dr$. As shown in Fig. 4, decreasing dt and dr leads to converged results, and a $dt = 10^{-4}$ s and a $n = 10$, which yield balance between accuracy and computational cost, are determined for the conditions C1 and C2. Besides, a $dt = 3 \times 10^{-5}$ s and a $n = 15$, which yield sufficient accuracy, are determined for the condition E0.

3.3. Single-layer melting simulation

Fig. 5(a) shows the illustration of ATM single-layer melting simulation and the line order scan strategy applied in this study. We selectively calculated the thermal field on target sections of interest by considering the heat accumulating effect of entire beam path in one layer. Here, the target sections in ATM simulations are defined as the regions containing the last several melting tracks within a divide unit that locates near the center of hatching area, as shown in Fig. 5(a). The target section has a thickness of 2 times the mesh size, i.e. 10 and 20 μm for E0 and others, respectively. Fig. 5(b) shows the melt layers mapped with the averaged G and R on the target sections simulated by ATM single-layer melting under the conditions C1, C2, and E0. Because of the relatively small or medium scan speed combined with the optimized line order scan strategy, the melting behaviors under the 3 different conditions consist of multiple individual melt pools propagating along scanning directions (this fact has been demonstrated in [17]). The last solidified areas in each individual melt pool exhibit smaller G and larger R than the areas near melt region boundaries under the 3 different conditions. Note the color scales of averaged G and R under the 3 conditions are different.

4. Model validation

Prior to discussing the grain structure evolution mechanisms based on the ATM simulation results, it is necessary to judge the limitations in ATM through comparing to the numerical models considering multi-physics in this study. The physics in each model are summarized in Table 2. Without the effect of fluid flow such as the Marangoni effect induced convection [25] transferring heat away from thermal center of melt pool, the width to depth ratio of single-track melt region simulated by ATM is smaller than that simulated by CFD as shown in Fig. 3(a-b). Although this width to depth ratio was not considered when determine beam parameters for ATM, the influences of physics (iv) and (v) in Table 2 on the magnitude of G and R are negligible because the FEM model, which ignored the physics (iv) and (v), yields G-R plots close to

those simulated by CFD as shown in Fig. 6(a). It should be noted that the G-R plots simulated by CFD include transient data extracted at each time step during the SSOI for each mesh on the central section normal to scanning direction, as shown in the Fig. 6(a), while those simulated by FEM and ATM employ averaged measure.

As shown in Fig. 6(a), despite the averaged G-R simulated by FEM under the condition C2 obviously shifts towards larger R comparing to C1, it is difficult to compare the transient G-R extracted at each time step during the SSOI simulated by CFD between the conditions C1 and C2. However, it should be noted that the G-R at the lower part of melt regions determine the bulk solidification grain structure in PBF-EB samples and that the averaged G-R at the lower part of melt regions simulated by CFD under the condition C2 are also shifted towards larger R comparing to C1, as shown in the sub-diagram of Fig. 6(a). This indicates that the dependence of averaged G-R at the lower part of melt regions on process parameters simulated by FEM is consistent with that simulated by CFD, and therefore, we consider that ignoring the physics (iv) and (v) is acceptable.

On the other hand, the averaged G-R simulated by ATM are apparently deviated from those simulated by FEM and CFD, as shown in Fig. 6(a-b). In order to analyze the main factors leading to this deviation, the FEM simulations were additionally performed in 2 cases of no latent heat (NLH) and no latent heat + temperature independent properties (NLH+TIP) under the condition C1. The effective energy absorption efficiency for the 2 cases was determined to 40%, which is smaller than 60% in the regular FEM case but close to 35% in the ATM as listed in Table 1, by fitting the FEM simulated single-track melt region depth to the experimental result. This indicates that the low effective energy absorption efficiency in ATM mainly attributes to ignoring the physics (ii), (iv), and (v) in Table 2. Besides, comparing to the G-R simulated by FEM, the deviation in the magnitude of averaged G-R simulated by ATM predominantly attributes to the effect of ignoring fusion latent heat, because the averaged G-R simulated by FEM-NLH and FEM-NLH+TIP are almost consistent with those simulated by ATM under the condition C1, as shown in the sub-diagram of Fig. 6(b). The dependence of averaged G-R on process conditions simulated by ATM is consistent with those simulated by CFD and FEM, i.e. the averaged G-R under condition C2 are shifted towards larger R compared to those under C1, indicating that the current ATM approach is capable to at least semi-quantitatively reveal the dependence of solidification conditions on process conditions.

Because R at the bottom of melt region can be geometrically linked to the scan speed (V), when the shape of melt pool reaches almost constant, as follows [26]:

$$R = V \times \cos\theta \quad (1a)$$

where θ is the deviation angle of the solidification front normal with respect to the scanning direction at melt pool bottom, and the condition C2 generates a very short melt pool with smaller θ than C2 as shown in Fig. 3(c), the geometrically deduced dependence of R on scan speed is consistent with those simulated by various models, i.e. $R_{C1} \approx 500 \text{ mm/s} \times \cos 88^\circ < 150 \text{ mm/s} \times \cos 82^\circ \approx R_{C2}$. This indicates that increasing scan speed does not necessarily tend to increase R.

5. Discussion

5.1. Non-steady-state CET mechanisms

The fundamental theories of solidification correlate the variations in solidification grain structure to the solidification conditions [27,28], and the solidification map, which maps solidification grain structure as a function of G and R, has been utilized

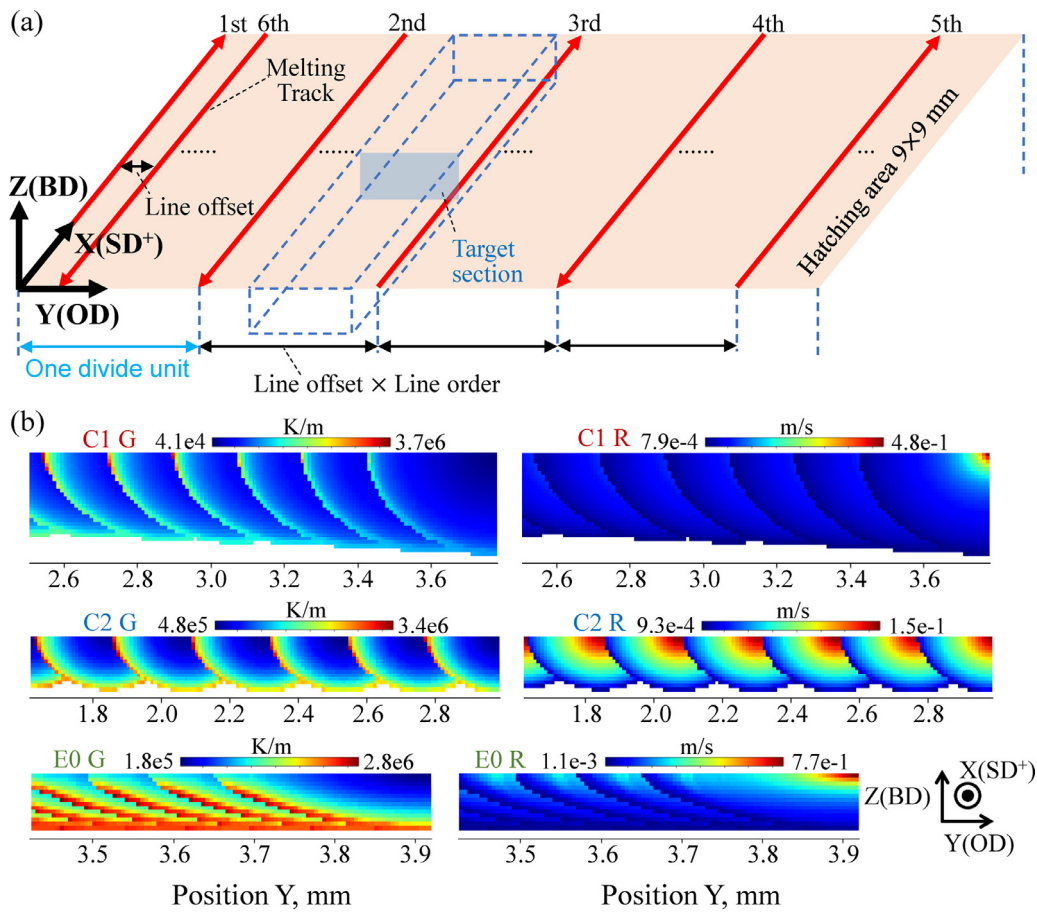


Fig. 5. (a) Illustration of the line order scan strategy and the target section of ATM single-layer melting simulation. (b) Melt layers overlapped by multiple single-track melt regions on the target sections simulated by ATM under the conditions C1, C2, and E0. The melt layers are mapped with averaged thermal gradient (G) and solidification rate (R) in each mesh. Each rightmost half melt region in (b) corresponds to the last one melting track in the corresponding divide unit. BD, OD, and SD⁺ denote building, offset and one of the scanning directions, respectively, during single-layer melting.

Table 2

Physics considered in the 3 kinds of simulations CFD, FEM, and ATM. ‘Y’ and ‘N’ denote consider and ignore the corresponding physic, respectively. NLH and TIP denote no latent heat and temperature-independent properties, respectively.

Physics	CFD	FEM	FEM		ATM
			NLH	NLH+TIP	
(i) Consider temperature-dependence of material properties	Y	Y	Y	N	N
(ii) Consider fusion latent heat	Y	Y	N	N	N
(iii) Do not assume half-infinite substrate	Y	Y	Y	Y	N
(iv) Consider radiation and vaporization	Y	N	N	N	N
(v) Consider fluid dynamics	Y	N	N	N	N

to discuss the solidification grain structure in PBF-EB built materials [12,14]. Fig. 7 shows a solidification map of Alloy713ELC and the plots of averaged G-R, which are calculated for the target sections indicated in Fig. 5(b) by using ATM single-layer melting simulation, under the conditions C1, C2, and E0. The solidification map was calculated with the nucleation volume density $N_0 = 10^{11} \text{ m}^{-3}$, through employing the steady-state CET models by Hunt [27], Kurz et al. [29], and Gäumann et al. [26], as mentioned in Appendix A.3. During single-layer melting, the heat accumulation induced by thermal-field superposition of adjacent tracks tends to decrease G, and therefore, the G-R plot of later tracks shift towards smaller G comparing to the former tracks, as indicated by the yellow arrows in Fig. 7, especially under the conditions C1 and E0 with relatively large scan speed. Besides, the R simulated by ATM single-layer melting follows $E0 > C2 > C1$, and this fact is consistent with those simulated by ATM single-track melting.

Despite the solidification grain structures under the conditions C1, C2, and E0 are distinctly different with each other in the experiment as mentioned in Section 3.1, their G-R plots at the lower part of melt layer simulated by ATM single-layer melting locate within the columnar zone in the solidification map, as shown in Fig. 7. The G-R plot of E0 is not closer to the equiaxed zone comparing to those of C1 and C2. Since the calculation of the bounds of the steady-state CET, i.e. the dotted curves in Fig. 6-7, is dependent on the calculation parameters mentioned in Appendix A.3, one cannot ignore the sensitivity of the steady-state CET, especially of the CET bound slope to calculation parameters, which may dramatically affect the rationalization of the variations in solidification grain structures between E0 and C1~2. Haines et al. [30] have systematically quantified the sensitivities of the steady-state CET to various calculation parameters under a context of Ni-base superalloy, and have revealed that the influence of the uncertainties in

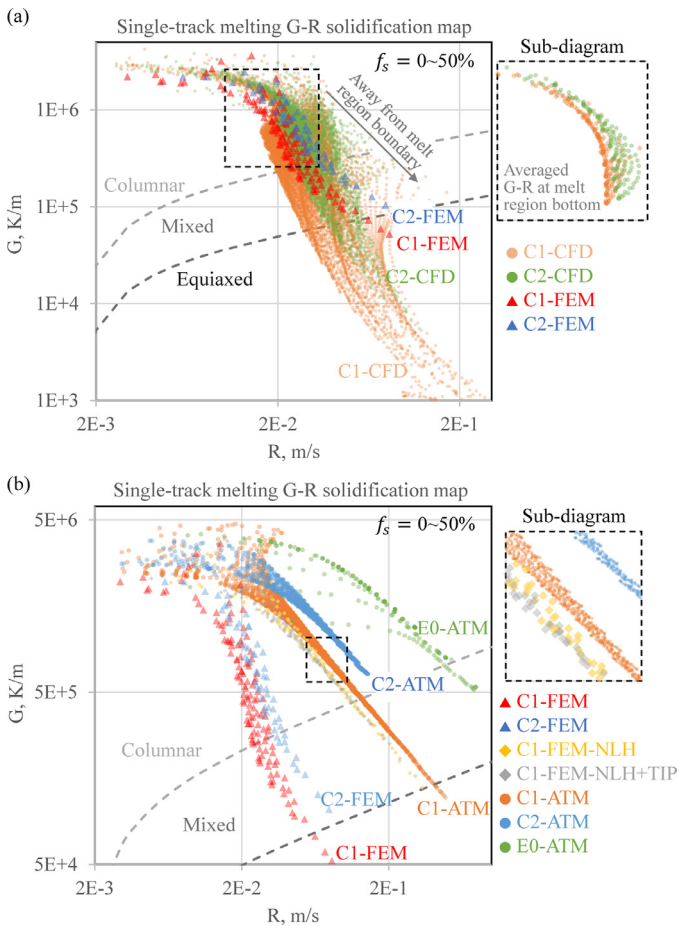


Fig. 6. Solidification maps with plots of thermal gradient (G) and solidification rate (R) during single-track melting under the conditions C1, C2, and E0 simulated with CFD, FEM, and ATM. NLH denotes no latent heat. TIP denotes temperature independent properties. f_s denotes solid fraction range under Scheil solidification employed for calculating G-R. Note the G-R are calculated with two kinds of measures, i.e. transient measure and averaged measure. See main text for details about the two kinds of measures. The FEM and ATM results apply averaged measure. The CFD results in the main-diagram of (a) apply transient measure, while those in the sub-diagram of (a) apply averaged measure. Note the transient G-R simulated by CFD include transient data extracted at each time step during the solidification stage of interest for each mesh. The dotted frames in (a & b) are accurately determined to indicate the scale of G-R in sub-diagrams. Note the axis scales of (a) are different from those of (b) and the G-R plots of C1-FEM and C2-FEM in (a) are consistent with those in (b).

calculation parameters on the slope of CET bound is neglectable compared to that on the intercept of CET bound, and that the influence of uncertainty in nucleation volume density N_0 on the intercept of CET bound is much greater than other calculation parameters. This indicates that the slope of the CET bound in Fig. 6–7 is acceptable and the steady-state CET model is insufficient to rationalize the variations in solidification grain structures between E0 and C1~2. Despite the intercept of the CET bound varies when calibrating N_0 , as is reported in [30,31], this aspect has little influence on the rationalization of the variations in solidification grain structures in this study.

In order to understand the CET mechanisms in this study, therefore, we still need to consider the aspects deviated from the steady-state CET model. The steady-state CET model assumes constant G direction (solidification direction) ahead of the columnar front [27] while the actual solidification in PBF-EB can be affected by the spatial and temporal variations of G direction. According to the widely accepted Walton and Chalmers selection model for the competitive growth [32], the columnar fronts of grains with a fa-

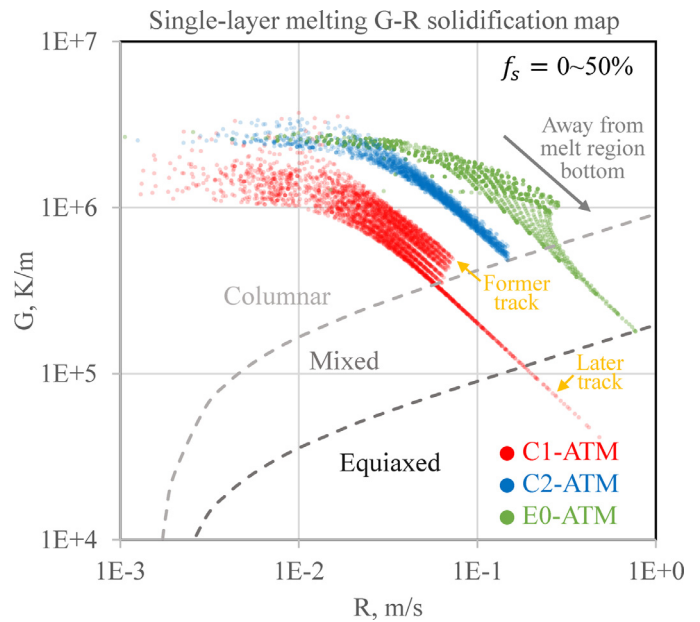


Fig. 7. A solidification map with plots of thermal gradient (G) and solidification rate (R) during the last solidification event on the target sections calculated with ATM single-layer melting simulation under the conditions C1, C2, and E0. f_s denotes solid fraction range under Scheil solidification employed for calculating G-R. Note G-R apply averaged measure. See main text for details about averaged measure.

vorable orientation, i.e. with preferential growth directions ($\langle 001 \rangle$ in this study) aligning closely with the G direction, can outgrow those of grains with a less favorable orientation, and most importantly, the latter exhibits a larger undercooling than the former [33].

The arrow plots in Fig. 8(a) indicate the G directions in melt layer on the target sections simulated by ATM single-layer melting under the conditions C1, C2, and E0. The color of arrows denotes the deviation angle of G direction with respect to the plane normal to scanning direction. The line order scan strategies under the 3 different conditions result in obviously different spatial variations of G direction. As shown in Fig. 8(a), since the scanning directions are opposite between adjacent melting tracks in each layer, the G directions swing back and forth with respect to the plane normal to scanning direction between the adjacent single-track melt regions (the color switches between reds and blues). Since both the C2 and E0 conditions generate short melt pools with steeper bottoms than C1, the swing induced by C2 and E0 exhibits deviation angles exceeding 15° while that induced by C1 exhibits deviation angles near 0° within the lower part of the melt layer, which is not re-melted during the processing of consequent layers.

Furthermore, the condition E0 generates shallow melt pools with a large width to depth ratio, leading to an overlapping effect, i.e. each melt layer is highly overlapped by multiple single-track melt regions along offset direction. Edge portions of 2~3 adjacent single-track melt regions with opposite swing orientation of G directions with respect to the plane normal to scanning direction, i.e. the local areas in reds or blues as shown by E0 in Fig. 8(a), are stacked along building direction within each layer. Therefore, we consider that the intrinsic spatial variations of G direction in each individual single-track melt region in conjunction with the overlapping effect can result in remarkable spatial and temporal variations of G direction, hindering the columnar growth in the PBF-EB sample E0. This argument is supported by the experimental result that some regions in the PBF-EB sample E0 exhibit zigzag shaped grains, as indicated by the arrows in Fig. 9(a). The zigzag shaped grains form when the G direction happens to wing from one of the

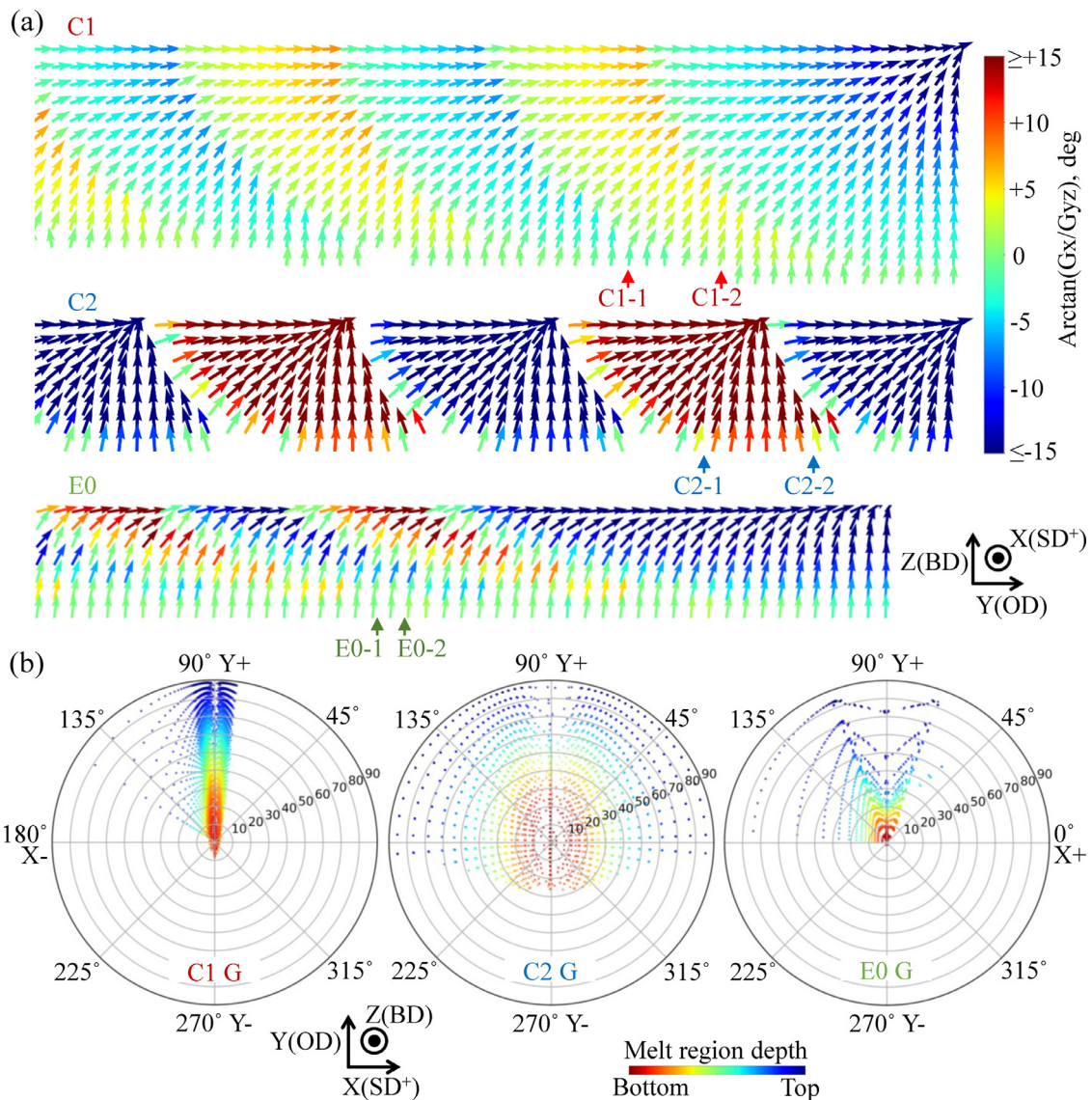


Fig. 8. (a) Arrow plots and (b) pole figures indicating the spatial variations and distributions of thermal gradient (G) direction during the last solidification event within one melt layer on the target sections. G directions are calculated with ATM single-layer melting simulation under the conditions C1, C2, and E0. BD, OD, and SD⁺ denote building, offset and one of the scanning directions, respectively, during single-layer melting.

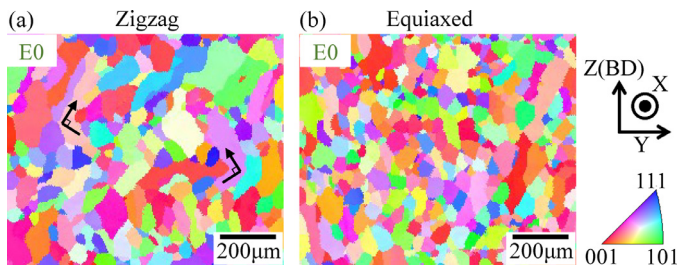


Fig. 9. Inverse pole figure (IPF) maps with reference to building direction (BD) of two kinds of grain structures at different positions in the PBF-EB sample E0: (a) zigzag and (b) equiaxed.

preferential growth directions {001} to another, as will be further discussed in Section 5.4. In other cases, we consider that the large undercooling ahead of the columnar front induced by the Walton and Chalmers selection effect can promote nucleation, and eventually, the frequently formed new grains impinging on the columnar

front can lead to a near fully equiaxed solidification grain structure, as shown in Fig. 9(b).

The Walton and Chalmers selection effect needs to be considered in conjunction with the effect of convection, because moderately increasing fluid velocity within the mushy zone can make the solute concentration curve steeper within the boundary layer ahead of solid-liquid interface, elevating the constitutional undercooling and detaching the existing dendrite arms to act as nuclei [34]. Fig. 3(c) and Fig. 10 show the fluid velocity within mushy zone and pure liquid zone calculated by CFD single-track melting simulations under the conditions C1 and C2. The mushy zone, which is treated as porous media corresponding to a primary dendrite arm spacing of 11.6 µm [16] in CFD, exhibits a much smaller fluid velocity than the liquid zone. The fluid velocity under the condition C2 is much larger within the mushy zone and slightly larger within the pure liquid zone than that under the condition C1, indicating that the shorter melt pools with a larger thermal gradient along melt pool top surface can lead to larger Marangoni force which results in stronger convection.

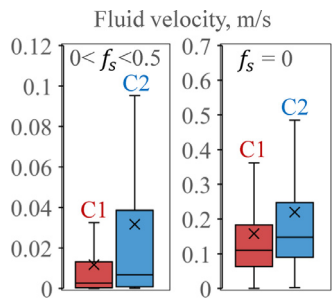


Fig. 10. Box plots of transient fluid velocities monitored on the central section normal to scanning direction at various time step within mushy zone ($0 < f_s < 0.5$) and pure liquid zone ($f_s = 0$). Fluid velocities are calculated with CFD single-track melting simulations under the conditions C1 and C2. f_s denotes solid fraction under Scheil solidification. The X spot is the mean value, the line within the box is the median value, the upper and lower box boundaries are the 3rd and 1st quartiles respectively, and the whiskers are the minimum and maximum values within 1.5 times the interquartile range from either boundary of the box.

Based on the above discussion, we define a non-steady-state CET as the CET that combines the steady-state CET [27,29] with the effect of spatial and temporal variations of G direction (i.e. the Walton and Chalmers selection effect [32]). In detail, we consider that a columnar growth predicted by the steady-state CET model in conjunction with the Walton and Chalmers selection effect and the effect of convection can promote nucleation to generate new grains ahead of columnar front, inducing a non-steady-state CET within each layer. This argument is supported by the fact that 50% areas in the PBF-EB sample E0 exhibit grain diameters below $80 \mu\text{m}$, which is smaller than the layer thickness of $100 \mu\text{m}$, as shown in Fig. 2(a). Eventually, the CET within each layer, coupled with the CET induced by the changes of G direction from one layer to the other as demonstrated by Körner et al. [7,8], result in the near fully equiaxed grain structure in the PBF-EB sample E0.

5.2. Columnar grain refining mechanisms

Understanding the non-steady-state CET mechanisms discussed in Section 5.1 helps us to reveal the columnar grain refining mechanisms in this study. The following discussion focuses on the lower part of melt layer because the lower part of melt layer, which is free from re-melting, determines the solidification grain structure in PBF-EB samples. The G directions in Fig. 8(a) are plotted to polar coordinates in Fig. 8(b). Fig. 8(a-b) reveal that the G directions at the lower part of melt layer under the condition C1 mainly align with the building direction and slightly point to the offset direction (Y+), while those under the condition C2 exhibit large deviation angles of G direction with respect to the building direction. This difference is also shown on the sections normal to offset direction at the various positions (C1-1 ~ C2-2 indicated by the arrows in Fig. 8(a)), which represent different patterns of the overlapping effect mentioned in Section 5.1. As shown in Fig. 11, the above statement about the condition C1 is true regardless of the Y-position. Therefore, the condition C1 is favorable for the epitaxial columnar growth along building direction. And the relatively weak (001) texture in scanning direction of PBF-EB sample C1 shown in Fig. 1(b) can attribute to the weak deflection of G direction to offset direction (Y+).

The difference between the conditions C2 and E0 is that C2 has a much larger line offset and a smaller width to depth ratio of melt pool than E0, and therefore, despite C2 has larger deviation angles of G direction with respect to the building direction than E0, E0 has a larger and more extensive overlapping effect than C2, as shown in Fig. 8(a-b). The spatial variations of G direction at the positions overlapped by single-track melt regions under the condition

C2, e.g. section C2-2 in Fig. 8(a) and Fig. 11, are similar with E0, while those at the positions not overlapped by single-track melt regions, e.g. section C2-1 in Fig. 8(a) and Fig. 11, are different from E0. Therefore, the condition C2 is insufficient to induce CET within the entire PBF-EB sample because the small overlapping fraction provides growing space for columnar grains. Nevertheless, those areas overlapped by single-track melt regions under the condition C2 are capable of forming new grains more frequently than C1. Besides, the strong deflection of G direction to scanning direction at the lower part of melt layer under the condition C2 leads to the stronger (001) texture in scanning directions than in C1, as shown in Fig. 1(b-c).

5.3. A method to manipulate non-steady-state CET in PBF-EB

Understanding the non-steady-state CET mechanisms that appeared in this study enables us to scheme a method to manipulate CET in PBF-EB by using a line order scan strategy optimized by the ATM simulation. Our basic idea for manipulating CET lies on that employing individual melt pools with a large width to depth ratio and steep bottoms in conjunction with a small line offset induces not only a deviation of G direction from building direction within the bottom of each melt pool but also an extensive overlapping effect within each melt layer, resulting in remarkable spatial variations of G direction along building direction, as shown by the E0 in Fig. 8(a) and Fig. 11. To achieve an appropriately large width to depth ratio of the melt pool, it is necessary to moderately increase focus offset according to beam current. Besides, the melt layer generated by the highly overlapped melt pools with steep bottoms and large width to depth ratio can lead to a V-shape in the scatter plot of G direction in polar coordinates, reflecting the real swing angle of G directions, as shown by the E0 in Fig. 8(b). Short melt pools are favorable for achieving steep bottoms and increasing the swing angle of G directions to an appropriate level that is capable of inducing either CET or zigzag growth.

The condition C2 is not capable of inducing CET extensively in the PBF-EB sample despite it leads to melt pools with steeper bottom than E0, indicating that the intrinsic spatial variations of G direction within each melt pool coupled with the changes of G direction from one layer to the other can be insufficient to manufacture bulk equiaxed solidification grain structure. The dash lines in Fig. 11 illustrate approximately the boundaries between the upper part that will be re-melted and the lower part that is free from re-melting of the melt layer under the 3 conditions, indicating that the fraction of the melt layer that is free from re-melting increases with decreasing P/V value. This implies that generating an appropriately shallow melt layer with ideal spatial variations of G direction within the lower part of melt layer that is free from re-melting is important for manufacturing near fully equiaxed PBF-EB samples with the current method.

It is worth mentioning that the highly overlapped melt regions applied in this method tend to accelerate heat accumulation. Therefore, an optimized line order scan strategy, which can disperse heat input, plays an important role. Besides, linking with our prior study regarding the thermo-mechanical effect in PBF-EB [17], we suggest that the total input energy should be tightly controlled as a function of scan speed to prevent hot cracking. Since the current method depends on multiple crucial process parameters, we propose that the guideline of manipulating CET is to determine high-dimensional process windows that satisfy the balance between several factors, i.e. (i) the swing angle of G direction induced by the overlapping effect discussed in Section 5.1, (ii) the melt layer depth, and (iii) the total plastic strain index reported in [17]. The factor (i) is discussed further in Section 5.4. An optimization, aiming at achieving the balance between the three factors,

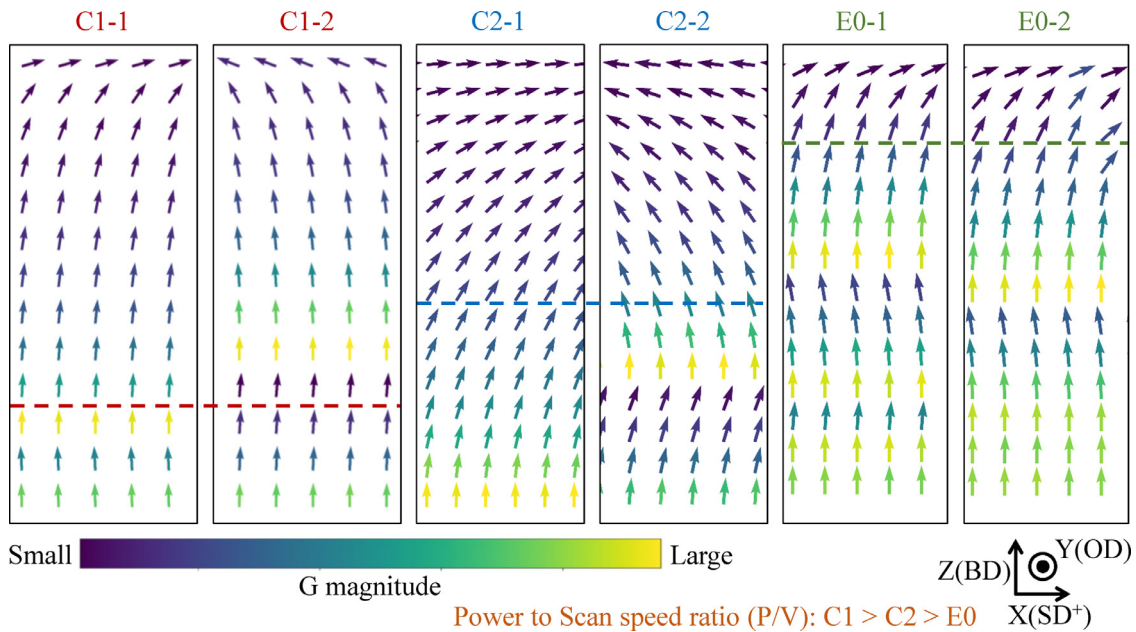


Fig. 11. Arrow plots showing the spatial variations of thermal gradient (G) direction during the last solidification event on the central XZ sections indicated in Fig. 8(a). G directions are calculated with ATM single-layer melting simulation under the conditions C1, C2, and E0. BD, OD, and SD^+ denote building, offset and one of the scanning directions, respectively, during single-layer melting.

should also take into account the advantage and the limitation discussed in Section 5.5.

As shown in Fig. 12, we have experimentally proved the capability of the current method to generate bulk solidification grain structures with either near fully equiaxed or interlocked zigzag shapes, through fabricating PBF-EB samples under the two kinds of process conditions, E1 and E2, which are modified from E0. Both the conditions E1 and E2 employ current 3.5 mA, scan speed 800 mm/s, line offset 40 μm , line order 100, and layer thickness 60 μm , with their only difference being that E1 applies focus offset of 30 mA while E2 applies that of 20 mA. The interlocked zigzag solidification grain structure is one kind of variant product acquired when adjusting electron beam focus, under the current method proposed to manipulate the non-steady-state CET.

5.4. Non-steady-state CET vs interlocked zig-zag growth

Rappaz et al. [35,36] have systematically studied the correlation between three factors: (i) the G direction, (ii) the crystallographic orientation of the dendrite within the mushy zone, and (iii) the growth velocity of the active $\langle 001 \rangle$ dendrite tip, during solidification for melt pool in FCC system. Their studies indicate that the transition of the active dendrite tip from one $\langle 001 \rangle$ to another occurs along some transition boundary lines (see [35,36]) that are as a function of the angle between G_y & G_{yz} , i.e. the deviation angle of the projection of G on the YZ-plane with respect to the Y-axis in Fig. 8(a), and the angle between G & G_{yz} , i.e. the deviation angles of G with respect to its projection on the YZ-plane in Fig. 8(a), for a given crystallographic orientation of dendrite, when ignoring the effect of non-steady-state CET. However, in the alloy systems that constitutional cooling may lead to nucleation, which is the case in the current study, one has to consider the effect of the transition boundary lines in conjunction with that of the non-steady-state CET. We deduce that the transition boundary lines in [35,36] can be dilated to transition boundary areas, which enlarge the minimum deviation angle of G with respect to the six $\langle 001 \rangle$ dendrite tips, and therefore, are the most likely to induce the non-steady-state CET. The non-steady-state CET occurs when the G direction swings into the transition boundary areas, whereas the zig-

zag growth occurs when the G direction swings skipping the transition boundary areas, with the width of the transition boundary areas depending on the alloy system.

Based on the above theory of transition boundary area, in order to rationalize the variations in solidification grain structure between E1 and E2, the following discussions will focus on the areas within each melt layer that do not suffer remelting and thus dominate the bulk solidification grain structure. Since the process parameters of the conditions E1 and E2 are similar to those of E0, the spatial and temporal variations of G direction of E1 and E2 should be similar to those of E0 shown in Fig. 8(a) to a certain extent. Given the effect of the electron beam focus on the melt pool geometry, as is discussed in Appendix A.1, one can deduce that the condition E2 has larger varying ranges than E1 for the angles between G_y & G_{yz} , and also for the angles between G & G_{yz} . This indicates that the condition C2 is statistically more likely than C1 to exhibit swings of G direction that skip the transition boundary areas, within the varying ranges for the angles between G_y & G_{yz} and the angles between G & G_{yz} , and consequently inducing a zig-zag growth. Besides, the interlocked zig-zag grain structure across multiple layers suggests that the swings of G direction within adjacent melt layers are well coupled to induce the interlocked zig-zag growth in the PBF-EB sample E2. This aspect needs to be further studied if one aims to establish process windows for the interlocked zig-zag growth.

5.5. Towards site-specific control of non-steady-state CET

The emerging science and technology of site-specific control of solidification grain structure in metallic components via PBF-AM have been greatly advanced in recent years, especially through the method by Dehoff et al. [10,11,37], employing the point heat source scan strategy to manipulate CET. Here, it is worth comparing the method proposed in this study for manipulating the non-steady-state CET, which is based on the line scan strategy, with the method based on the point heat source scan strategy. Raplee et al. [37] have reported that the point melt region exhibits a much coarser primary dendrite arm spacing than the line melt region, which can be rationalized by the theoretical predictions by Ragha-

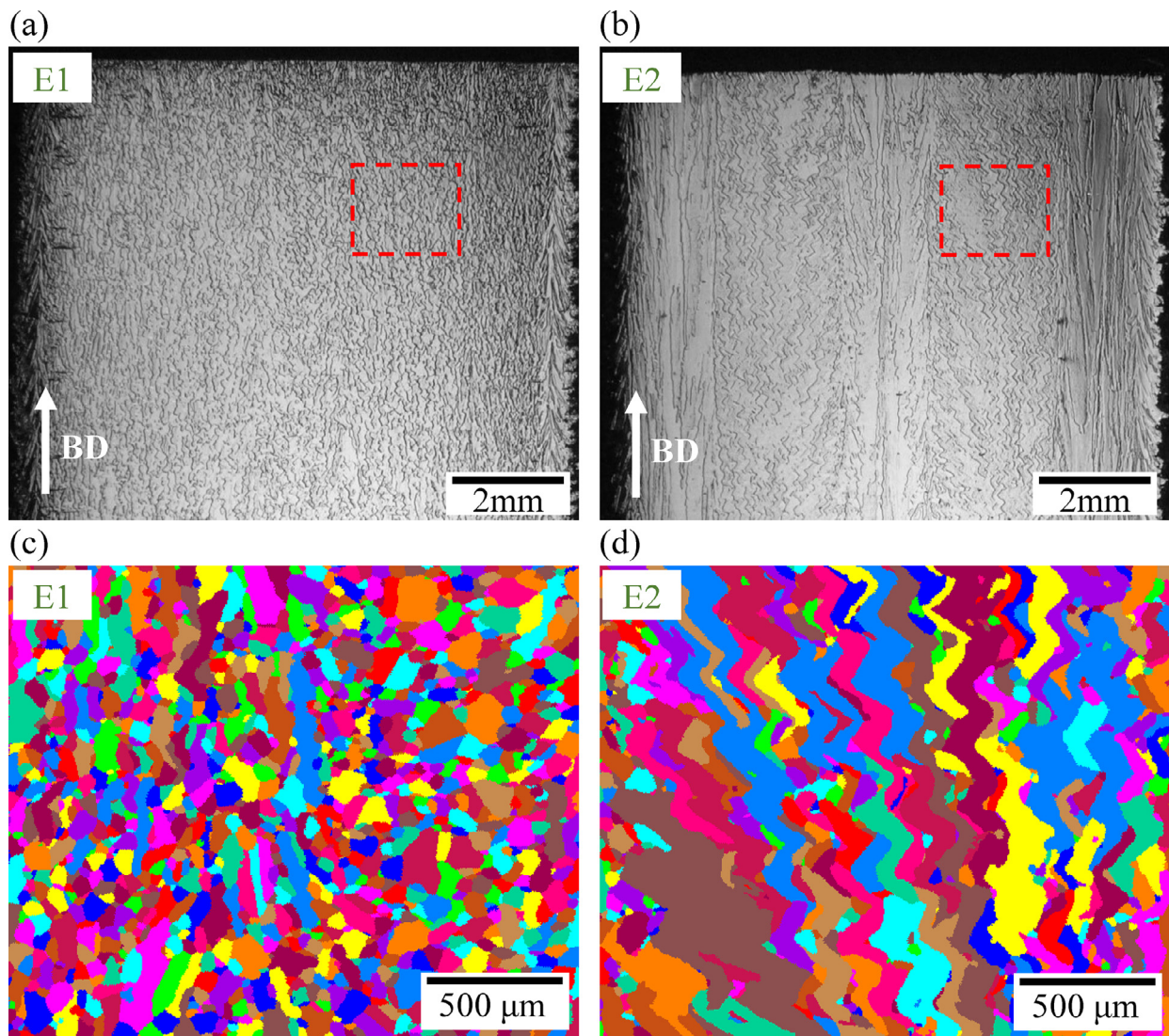


Fig. 12. Two kinds of bulk solidification grain structures created by using the method proposed in this study under the conditions E1 and E2: (a & c) near fully equiaxed and (b & d) interlocked zigzag structures. (a-b) Optical microscope photos of the entire central vertical sections of the upper parts of the PBF-EB samples. (c-d) EBSD grain maps captured at approximately the areas indicated by dotted frames in (a-b). BD denotes building direction.

van et al. [14] based on the Kurz-Fisher model [38]. This indicates that an advantage of the method proposed in this study is that, being capable of creating bulk equiaxed grain structures with a much finer substructure compared to those generated by the point heat source scan strategy. This aspect should rely on the quantitative control of G and R . Since the solidification grain structure created by the non-steady-state CET are distinct from that created by the steady-state CET, the microstructural and mechanical characteristics for the non-steady-state CET will be studied in future.

On the other hand, Frederick et al. [31] have revealed that the solidification conditions under the line scan strategies are actually functions of not only the process parameters but also the hatching area geometries. Therefore, a major challenge in the current method for site-specific control of the non-steady-state CET could be to achieve consistent solidification microstructure across hatching areas with complex geometry, compared to the method based on the point heat source scan strategy which does not have this limitation [10,11]. Besides, given that the conditions E0 and E1 rely on a significant heat accumulation effect to generate sufficient melt layer depths, as mentioned in Appendix A.1, future approaches to advance the current method can be either to search process win-

dows for the non-steady-state CET on the premise of minimized heat accumulation effect, or to develop algorithms for the management of heat accumulation.

6. Conclusion

We proposed a method for site-specific control of solidification grain structure through controlling process parameters under a line order scan strategy in PBF-EB. Through fabricating PBF-EB samples under optimized conditions, we have demonstrated the capability of this method to manipulate the solidification grain structure of Alloy713ELC into (i) near fully equiaxed structure with highly weak texture, (ii) interlocked zigzag structure, or (iii) columnar structure with various grain width. The solidification grain structure evolution mechanisms under this method are summarized below:

- (1) Single-layer melting simulations reveal that the spatial variations of solidification direction within each individual single-track melt region, in conjunction with the overlapping effect of adjacent single-track melt regions, have a significant influence on the solidification grain structure.

- (2) Appropriately decreasing the deviation angle of solidification direction with respect to the scanning direction at melt pool bottom helps to induce spatial variations of solidification direction between adjacent single-track melt regions within each layer. Moderately decreasing the depth of melt layer tends to increase the fraction of melt layer that is free from re-melting during the processing of consequent layers, and thus, helps to retain the spatial variations of solidification direction in the solidification grain structure.
- (3) An optimized line order scan strategy with a moderately large focus offset and a small line offset, leading to multiple individual melt pools with a large width to depth ratio and steep bottoms, generates a highly overlapped melt layer with remarkable local spatial variations of solidification direction along building direction. Depending on the swing angle of thermal gradient direction and the transition boundary areas, the local spatial variations of solidification direction can either induce a significant Walton and Chalmers selection effect within each melt layer or induce interlocked zigzag growth.
- (4) The Walton and Chalmers selection effect combined with the effect of large convection in short melt pools leads to a large constitutional undercooling at columnar fronts, which is capable of promoting nucleation and eventually inducing non-steady-state CET in PBF-EB.
- (5) The non-steady-state CET defined in this study is important in the solidification grain structure evolution mechanisms in PBF-EB.

Declaration of Competing Interest

The authors declare that they have no known competing financial interests or personal relationships that could have appeared to influence the work reported in this paper.

Acknowledgments

This work was supported by the inter-university cooperative research program (Proposal No. 18G0418, 19G0411, and 20G0418) of the Cooperative Research and Development Center for Advanced Materials, Institute for Materials Research, Tohoku University. This study was also based on the results obtained from a project, JPNP19007, commissioned by the New Energy and Industrial Technology Development Organization (NEDO). This work was also partly supported by JSPS KAKENHI (Grant Number 18H03834). The powders for PBF-EB were supplied by Global Research & Innovative Technology Center (GRIT), Hitachi Metals, Ltd. One of the authors, Yuchao Lei, was financially supported by the Amano Institute of Technology Scholarship.

Supplementary materials

Supplementary material associated with this article can be found, in the online version, at doi:[10.1016/j.actamat.2022.117717](https://doi.org/10.1016/j.actamat.2022.117717).

References

- [1] W.E. Frazier, Metal additive manufacturing: a review, *J. Mater. Eng. Perform.* 23 (2014) 1917–1928, doi:[10.1007/s11665-014-0958-z](https://doi.org/10.1007/s11665-014-0958-z).
- [2] R. Huang, M. Riddle, D. Graziano, J. Warren, S. Das, S. Nimbalkar, J. Cresko, E. Masanet, Energy and emissions saving potential of additive manufacturing: the case of lightweight aircraft components, *J. Clean. Prod.* 135 (2016) 1559–1570, doi:[10.1016/j.jclepro.2015.04.109](https://doi.org/10.1016/j.jclepro.2015.04.109).
- [3] M. Ramsperger, C. Körner, Selective electron beam melting of the single crystalline nickel-base superalloy CMSX-4®: from columnar grains to a single crystal, in: *Proc. Int. Symp. Superalloys, 2016*, pp. 341–349, doi:[10.1002/9781119075646.ch37](https://doi.org/10.1002/9781119075646.ch37).
- [4] C. Körner, M. Ramsperger, C. Meid, D. Bürger, P. Wollgramm, M. Bartsch, G. Eggeler, Microstructure and Mechanical Properties of CMSX-4 Single Crystals Prepared by Additive Manufacturing, *Metall. Mater. Trans. A* 49 (2018) 3781–3792, doi:[10.1007/s11661-018-4762-5](https://doi.org/10.1007/s11661-018-4762-5).

- [5] E. Chauvet, C. Tassin, J.-J. Blandin, R. Dendievel, G. Martin, Producing Ni-base superalloys single crystal by selective electron beam melting, *Scr. Mater.* 152 (2018) 15–19, doi:[10.1016/j.scriptamat.2018.03.041](https://doi.org/10.1016/j.scriptamat.2018.03.041).
- [6] P. Fernandez-Zelada, M.M. Kirka, A.M. Rossy, Y. Lee, S.N. Dryepondt, Nickel-based superalloy single crystals fabricated via electron beam melting, *Acta Mater* (2021), doi:[10.1016/j.actamat.2021.117133](https://doi.org/10.1016/j.actamat.2021.117133).
- [7] C. Körner, H. Helmer, A. Bauereiß, R.F. Singer, Tailoring the grain structure of IN718 during selective electron beam melting, *MATEC Web Conf.*, 2014, doi:[10.1051/mateconf/20141408001](https://doi.org/10.1051/mateconf/20141408001).
- [8] H. Helmer, A. Bauereiß, R.F. Singer, C. Körner, Grain structure evolution in Inconel 718 during selective electron beam melting, *Mater. Sci. Eng. A* (2016), doi:[10.1016/j.msea.2016.05.046](https://doi.org/10.1016/j.msea.2016.05.046).
- [9] R.R. Dehoff, M.M. Kirka, F.A. List, K.A. Unocic, W.J. Sames, Crystallographic texture engineering through novel melt strategies via electron beam melting: inconel 718, *Mater. Sci. Technol. (United Kingdom)* (2015), doi:[10.1179/1743284714Y.0000000697](https://doi.org/10.1179/1743284714Y.0000000697).
- [10] R.R. Dehoff, M. Kirka, W.J. Sames, H. Bilheux, A.S. Tremsin, L.E. Lowe, S.S. Babu, Site specific control of crystallographic grain orientation through electron beam additive manufacturing, *Mater. Sci. Technol. (United Kingdom)* (2015), doi:[10.1179/1743284714Y.0000000734](https://doi.org/10.1179/1743284714Y.0000000734).
- [11] A. Plotkowski, J. Ferguson, B. Stump, W. Halsey, V. Paquit, C. Joslin, S.S. Babu, A. Marquez Rossy, M.M. Kirka, R.R. Dehoff, A stochastic scan strategy for grain structure control in complex geometries using electron beam powder bed fusion, *Addit. Manuf.* 46 (2021) 102092, doi:[10.1016/j.addma.2021.102092](https://doi.org/10.1016/j.addma.2021.102092).
- [12] N. Raghavan, R. Dehoff, S. Pannala, S. Simunovic, M. Kirka, J. Turner, N. Carlson, S.S. Babu, Numerical modeling of heat-transfer and the influence of process parameters on tailoring the grain morphology of IN718 in electron beam additive manufacturing, *Acta Mater* (2016), doi:[10.1016/j.actamat.2016.03.063](https://doi.org/10.1016/j.actamat.2016.03.063).
- [13] P. Kontis, E. Chauvet, Z. Peng, J. He, A.K. da Silva, D. Raabe, C. Tassin, J.-J. Blandin, S. Abed, R. Dendievel, B. Gault, G. Martin, Atomic-scale grain boundary engineering to overcome hot-cracking in additively-manufactured superalloys, *Acta Mater* 177 (2019) 209–221, doi:[10.1016/j.actamat.2019.07.041](https://doi.org/10.1016/j.actamat.2019.07.041).
- [14] N. Raghavan, S. Simunovic, R. Dehoff, A. Plotkowski, J. Turner, M. Kirka, S. Babu, Localized melt-scan strategy for site specific control of grain size and primary dendrite arm spacing in electron beam additive manufacturing, *Acta Mater* (2017), doi:[10.1016/j.actamat.2017.08.038](https://doi.org/10.1016/j.actamat.2017.08.038).
- [15] Y. Zhao, Y. Koizumi, K. Aoyagi, D. Wei, K. Yamanaka, A. Chiba, Comprehensive study on mechanisms for grain morphology evolution and texture development in powder bed fusion with electron beam of Co–Cr–Mo alloy, *Materialia* (2019), doi:[10.1016/j.mta.2019.100346](https://doi.org/10.1016/j.mta.2019.100346).
- [16] Y. Lei, K. Aoyagi, Y. Cui, D.-S. Kang, K. Kuwabara, K. Aota, A. Chiba, Process optimization and mechanical property investigation of non-weldable superalloy Alloy713ELC manufactured with selective electron beam melting, *Mater. Sci. Eng. A* 787 (2020), doi:[10.1016/j.msea.2020.139485](https://doi.org/10.1016/j.msea.2020.139485).
- [17] Y. Lei, K. Aoyagi, K. Aota, K. Kuwabara, A. Chiba, Critical factor triggering grain boundary cracking in non-weldable superalloy Alloy713ELC fabricated with selective electron beam melting, *Acta Mater* (2021), doi:[10.1016/j.actamat.2021.116695](https://doi.org/10.1016/j.actamat.2021.116695).
- [18] K. Aoyagi, H. Wang, H. Sudo, A. Chiba, Simple method to construct process maps for additive manufacturing using a support vector machine, *Addit. Manuf.* 27 (2019) 353–362, doi:[10.1016/j.addma.2019.03.013](https://doi.org/10.1016/j.addma.2019.03.013).
- [19] A. Plotkowski, M.M. Kirka, S.S. Babu, Verification and validation of a rapid heat transfer calculation methodology for transient melt pool solidification conditions in powder bed metal additive manufacturing, *Addit. Manuf.* 18 (2017) 256–268, doi:[10.1016/j.addma.2017.10.017](https://doi.org/10.1016/j.addma.2017.10.017).
- [20] R. Forslund, A. Snis, S. Larsson, Analytical solution for heat conduction due to a moving Gaussian heat flux with piecewise constant parameters, *Appl. Math. Model.* (2019), doi:[10.1016/j.apm.2018.09.018](https://doi.org/10.1016/j.apm.2018.09.018).
- [21] E.J. Schwalbach, S.P. Donegan, M.G. Chapman, K.J. Chaput, M.A. Groeber, A discrete source model of powder bed fusion additive manufacturing thermal history, *Addit. Manuf.* (2019), doi:[10.1016/j.addma.2018.12.004](https://doi.org/10.1016/j.addma.2018.12.004).
- [22] J.C. Steuben, A.J. Birnbaum, J.G. Michopoulos, A.P. Iliopoulos, Enriched analytical solutions for additive manufacturing modeling and simulation, *Addit. Manuf.* (2019), doi:[10.1016/j.addma.2018.10.017](https://doi.org/10.1016/j.addma.2018.10.017).
- [23] B. Stump, A. Plotkowski, An adaptive integration scheme for heat conduction in additive manufacturing, *Appl. Math. Model.* 75 (2019) 787–805, doi:[10.1016/j.apm.2019.07.008](https://doi.org/10.1016/j.apm.2019.07.008).
- [24] R. Komanduri, Z.B. Hou, Thermal analysis of the arc welding process: part I. General solutions, *Metall. Mater. Trans. B Process Metall. Mater. Process. Sci.* (2000), doi:[10.1007/s11663-000-0022-2](https://doi.org/10.1007/s11663-000-0022-2).
- [25] Y. Zhao, Y. Koizumi, K. Aoyagi, D. Wei, K. Yamanaka, A. Chiba, Molten pool behavior and effect of fluid flow on solidification conditions in selective electron beam melting (SEBM) of a biomedical Co–Cr–Mo alloy, *Addit. Manuf.* 26 (2019) 202–214, doi:[10.1016/j.addma.2018.12.002](https://doi.org/10.1016/j.addma.2018.12.002).
- [26] M. Gäumann, C. Bezençon, P. Canalis, W. Kurz, Single-crystal laser deposition of superalloys: processing-microstructure maps, *Acta Mater* (2001), doi:[10.1016/S1359-6454\(00\)00367-0](https://doi.org/10.1016/S1359-6454(00)00367-0).
- [27] J.D. Hunt, Steady state columnar and equiaxed growth of dendrites and eutectic, *Mater. Sci. Eng.* 65 (1984) 75–83, doi:[10.1016/0025-5416\(84\)90201-5](https://doi.org/10.1016/0025-5416(84)90201-5).
- [28] W. Kurz, C. Bezençon, M. Gäumann, Columnar to equiaxed transition in solidification processing, *Sci. Technol. Adv. Mater.* 2 (2001) 185–191, doi:[10.1016/S1468-6996\(01\)00047-X](https://doi.org/10.1016/S1468-6996(01)00047-X).
- [29] W. Kurz, B. Giovanola, R. Trivedi, Theory of microstructural development during rapid solidification, *Acta Metall* (1986), doi:[10.1016/0001-6160\(86\)90056-8](https://doi.org/10.1016/0001-6160(86)90056-8).
- [30] M. Haines, A. Plotkowski, C.L. Frederick, E.J. Schwalbach, S.S. Babu, A sensitivity analysis of the columnar-to-equiaxed transition for Ni-based super-

- alloys in electron beam additive manufacturing, *Comput. Mater. Sci.* (2018), doi:[10.1016/j.commatsci.2018.08.064](https://doi.org/10.1016/j.commatsci.2018.08.064).
- [31] C.L. Frederick, A. Plotkowski, M.M. Kirka, M. Haines, A. Staub, E.J. Schwalbach, D. Cullen, S.S. Babu, Geometry-Induced Spatial Variation of Microstructure Evolution During Selective Electron Beam Melting of Rene-N5, *Metall. Mater. Trans. A Phys. Metall. Mater. Sci.* (2018), doi:[10.1007/s11661-018-4793-y](https://doi.org/10.1007/s11661-018-4793-y).
- [32] D. Walton, B. Chalmers, The origin of the preferred orientation in the columnar zone of ingots, *Trans. Am. Inst. Min. Metall. Eng.* 215 (1959) 447–457.
- [33] M. Rappaz, C.A. Gandin, Probabilistic modelling of microstructure formation in solidification processes, *Acta Metall. Mater.* (1993), doi:[10.1016/0956-7151\(93\)90065-Z](https://doi.org/10.1016/0956-7151(93)90065-Z).
- [34] J. Hutt, D. StJohn, The origins of the equiaxed zone -Review of theoretical and experimental work, *Int. J. Cast Met. Res.* (1998), doi:[10.1080/13640461.1998.11819254](https://doi.org/10.1080/13640461.1998.11819254).
- [35] M. Rappaz, S.A. David, J.M. Vitek, L.A. Boatner, Development of microstructures in Fe-15Ni-15Cr single crystal electron beam welds, *Metall. Trans. A.* (1989), doi:[10.1007/BF02650147](https://doi.org/10.1007/BF02650147).
- [36] M. Rappaz, S.A. David, J.M. Vitek, L.A. Boatner, Analysis of solidification microstructures in Fe-Ni-Cr single-crystal welds, *Metall. Trans. A.* (1990), doi:[10.1007/BF02672593](https://doi.org/10.1007/BF02672593).
- [37] J. Raplee, A. Plotkowski, M.M. Kirka, R. Dinwiddie, A. Okello, R.R. Dehoff, S.S. Babu, Thermographic Microstructure Monitoring in Electron Beam Additive Manufacturing, *Sci. Rep.* (2017). doi:[10.1038/srep43554](https://doi.org/10.1038/srep43554).
- [38] W. Kurz, D.J. Fisher, Dendrite growth at the limit of stability: tip radius and spacing, *Acta Metall* (1981), doi:[10.1016/0001-6160\(81\)90082-1](https://doi.org/10.1016/0001-6160(81)90082-1).